

The eye of Gaia on globular clusters structure: tidal tails

A. Sollima^{1*}

¹ *INAF Osservatorio di Astrofisica e Scienza dello spazio di Bologna, via Gobetti 93/3, 40129 Bologna, Italy*

Accepted 2020 April 25. Received 2020 April 22; in original form 2020 January 23

ABSTRACT

I analyse the projected density distribution of member stars over a wide area surrounding 18 Galactic globular clusters using the photometric and astrometric information provided by the second data release of the Gaia mission. A 5D mixture modelling technique has been employed to optimally isolate the signal of the cluster stellar population from the contamination of the Galactic field, taking advantage of its different distribution in the space formed by colours, magnitudes, parallaxes and proper motions. In 7 clusters I detect collimated overdensities at a $> 3 \sigma$ level above the background density extending well beyond the cluster tidal radius, consistent with the distortion expected as a result of the tidal interaction with the Milky Way potential. In five of these clusters (NGC288, NGC2298, NGC5139, NGC6341 and NGC7099) spectacular tidal tails extend up to the border of the analysed field of view at 5 degrees from the centre. At large distances from the cluster centre, the orientation of the detected overdensities appears to be systematically aligned with the cluster orbital path, in agreement with the predictions of N-body simulations. The fraction of stars contained in the tidal tails of these clusters is also used to determine the first observational estimate of their present-day destruction rates.

Key words: methods: statistical – stars: kinematics and dynamics – stars: Population II – globular clusters: general

1 INTRODUCTION

Any stellar system immersed in a gravitational potential is subject to its tidal strain. In particular, the presence of the external potential introduces a repulsive centrifugal term which adds to the internal gravitational potential and determines an anisotropic shape of the effective potential contours. The effect of tidal distortion is more pronounced at large distances from the center where tidal forces dominates over the internal gravitation. Globally, the zero-velocity surfaces have a characteristic elongated shape (Roche lobe) with two saddle points (the so-called "Lagrangian points", located at a distance from the cluster centre called "Jacobi radius") and aligned with the direction of the galactic potential gradient (i.e. toward the galactic centre; Binney & Tremaine 1987). Stellar orbits confined in the outer region of the stellar system are therefore distorted toward the Lagrangian points and the stellar density follows the shape of the Roche lobe. A star with orbital energy exceeding the effective potential at the Lagrangian points can escape from the system if its orbit crosses an aperture around these points, whose size depends on its energy excess (Fukushige & Heggie 2000). Once escaped, the star initially moves away from the satel-

lite following the path along its escape direction i.e. radially along the satellite-galactic centre direction. As the distance of the star increases, the Coriolis force becomes significant pushing the star toward the same orbital path of its original stellar system. The appearance of the whole system is therefore characterised by the presence of a pair of symmetric tails emerging from the satellite and following a S-shape (Montuori, et al. 2007; Klimontowski, et al. 2009). The stars in the tidal tails become independent satellites with integrals of motion similar to those of their original host stellar system, and therefore follow its orbit with a slightly different orbital period. Stars escaped at early epochs accumulate a large phase delay and are therefore more distant from the satellite than those recently escaped. So, the orientation and prominence of tidal tails provide crucial information on the orbit and the recent mass-loss history of a stellar system.

Examples of tidal features have been observed in interacting galaxies (Duc, et al. 2015) and around the most recent accretion events occurred in the Milky Way and M31 (Ibata, Gilmore & Irwin 1994; Ibata, et al. 2001). All these systems are characterised by large mass-loss rates (up to $10^8 \text{ stars Gyr}^{-1}$; Fardal, et al. 2006; Law & Majewski 2010) leaving observational features easily detectable with imaging techniques as surface brightness or star counts excess (Belokurov, et al. 2006a; Martínez-Delgado, et al. 2010).

* E-mail: antonio.sollima@inaf.it

The detection of tidal tails is more challenging in star clusters, characterised by a significantly smaller mass-loss rate ($\sim 10^{2\pm 4}$ stars Gyr^{-1} ; Dinescu, Girard & van Altena 1999). The stars in the tails constitute indeed a tiny fraction ($< 0.1\%$) of those contained in the region surrounding the cluster, mainly populated by Galactic interlopers. For this reason, filtering techniques are used to maximize the signal of the cluster by assigning weights to stars according to their position in the colour-magnitude diagram (the "matched-filter"; Rockosi, et al. 2002). Thanks to this techniques, it has been possible to detect tidal features around many globular (GCs; Grillmair, et al. 1995; Leon, Meylan & Combes 2000; Chun, et al. 2010; Chen & Chen 2010; Jordi & Grebel 2010; Chun, et al. 2015; Shipp, et al. 2018; Carballo-Bello, et al. 2018) and open clusters (Bergond, Leon & Guibert 2001; Dalessandro, et al. 2015). Most of these studies discovered only deformations of the density contours close to the clusters' tidal radii interpreted as the result of tidal effects. Spectacular exceptions are constituted by the 30° -long tail detected around Palomar 5 (Odenkirchen, et al. 2001; Erkal, Koposov & Belokurov 2017) and, to a less extent, the tidal tails detected in NGC 5466 (Belokurov, et al. 2006b), Palomar 1, (Niederste-Ostholt, et al. 2010), Palomar 14 (Sollima, et al. 2011), Eridanus and Palomar 15 (Myeong, et al. 2017) and NGC 7492 (Navarrete, Belokurov & Koposov 2017).

The 2nd data release of the Gaia mission (Gaia Collaboration, et al. 2018a) recently provided (beside colours and magnitudes) parallaxes and proper motions for $\sim 1.3 \times 10^9$ stars across the entire sky, allowing to increase the number of dimensions of the parameter space where to select cluster members. Thanks to this dataset it has been possible to detect extended tidal tails in NGC5139 (Ibata, et al. 2019a), NGC288 (Kaderali, et al. 2019), NGC362 (Carballo-Bello 2019), NGC3201 (Bianchini, Ibata & Famaey 2019), NGC5904 (Grillmair 2019) and around a few open clusters (Röser, Schilbach & Goldman 2019; Röser & Schilbach 2019; Tang, et al. 2019).

In this paper I perform a systematic search for tidal tails around a sample of 18 nearby GCs using the full 5D parameter space provided by Gaia data. In Sect. 2 the analysed sample of GCs, together with the description of the adopted dataset is presented. The algorithm adopted to determine the projected density map is described in Sect. 3 and the results of the analysis are presented in Sect. 4. Finally, the conclusions are presented in Sect. 5.

2 OBSERVATIONAL MATERIAL

2.1 GC sample

The GCs analysed in this paper have been selected as those with the largest probability of detection of low-surface brightness features. Many factors affect this probability, among them: *i*) the amount of mass lost in recent epochs, *ii*) the fraction of the cluster stellar population sampled by the adopted catalog, *iii*) the density of Galactic field stars, and *iv*) the separation of cluster and field stars in the considered parameter space.

Table 1. GCs analysed in this work (column (1)). The detection of significant tidal tails, according to the criteria described in Sect. 4.1 is reported in column (2) and the destruction rate, where available, is listed in column (3).

| NGC | tidal tails | ν Gyr^{-1} |
|------|-------------|---------------------|
| 288 | Y | 0.033±0.003 |
| 1851 | N | |
| 1904 | N | |
| 2298 | Y | 0.057±0.007 |
| 2808 | N | |
| 3201 | N | |
| 4590 | N | |
| 5139 | Y | 0.019±0.002 |
| 5272 | N | |
| 5897 | N | |
| 5904 | Y | |
| 6205 | N | |
| 6341 | Y | 0.018±0.001 |
| 6362 | Y | |
| 6752 | N | |
| 7078 | N | |
| 7089 | N | |
| 7099 | Y | 0.085±0.004 |

Although theoretical predictions of the mass-loss rate of GCs exist in the literature (Gnedin & Ostriker 1997; Allen, Moreno & Pichardo 2006), many uncertainties affect these estimates (due to the uncertainties in the adopted Galactic potential, GC space velocities, recipes for mass loss, etc.). So no selection has been made on the basis of this parameter. On the other hand, even in case of large mass loss rates, the tidal tails of low-mass and/or distant GCs will be sampled only with a small number of stars. For this reason, I excluded GCs with integrated apparent magnitude $V > 9.5$.

The fraction of sampled cluster stellar population depends mainly on the fraction of Main Sequence stars brighter than the limiting magnitude of Gaia and therefore on the cluster heliocentric distance. The GCs analysed here were selected among those at distances $d_\odot < 15$ kpc (from Harris 1996, 2010 edition). Considering the Gaia limiting magnitude ($20 < G_{cut} < 21$; see Sect. 2.2), this corresponds to ~ 1 magnitude below the turn-off of a typical old and metal-poor ($t > 10$ Gyr; $[Fe/H] < -1$) GC stellar population (Bressan, et al. 2012).

To limit the fraction of Galactic disc and bulge interlopers, I excluded those GCs lying at latitudes $|b| < 10^\circ$ and at a projected distance from the Galactic centre $R_{GC} < 30^\circ$. I also excluded NGC104 and NGC362 because of the contamination from Small Magellanic Cloud stars in the background of these clusters.

Some nearby GCs, in spite of their projected position in the sky, have a mean proper motions significantly different from that of the surrounding Galactic population. The stellar population of these GCs can be easily isolated allowing an efficient analysis. Among these GCs I included in the sample NGC3201 (with a systemic proper motion different by $\Delta\mu \sim 14$ mas yr^{-1} from the mean proper motion of the field population), in spite of its low latitude ($b = 8^\circ.64$).

Instead, the GC NGC5286 has been excluded because of the extremely high small-scale spatial variation of the Gaia

catalog completeness even at bright magnitudes ($G_{cut} < 20$; see Sect. 2.2).

The final sample consists of 18 GCs (see Table 1), $\sim 12\%$ of the entire Milky Way GC system, and constitutes one of the most extensive sample adopted for this kind of studies.

2.2 Gaia catalog selection

The analysis performed here is entirely based on data provided by the Gaia 2nd data release (Gaia Collaboration, et al. 2018a). This survey measured parallaxes, proper motions, magnitudes and colours for 1.3×10^9 stars in the entire sky, including almost all known Galactic GCs in both hemispheres. The catalog has a formal limiting magnitude of $G = 21$, although this value depends on celestial position. Moreover, the source completeness varies with a patchy structure characterised by source density fluctuations that reflect the scan law pattern of the survey (Arenou et al. 2018).

For each GC, the full set of information of all sources contained in a circle with radius of 5° centered on the GC centre has been retrieved. It consists of G magnitudes, $G_{BP} - G_{RP}$ colours, parallaxes (p), proper motions (μ_α^* , μ_δ) together with their associated uncertainties and corresponding covariances. Uncertainties in parallaxes have been corrected using the prescriptions of Lindegren, et al. (2018). The G magnitudes and $G_{BP} - G_{RP}$ colours have been corrected for interstellar extinction using the reddening maps of Lallement et al. (2019)¹ and the extinction coefficients by Casagrande & VandenBerg (2018).

To maximize the detection efficiency avoiding to introduce any bias, no selection has been made on the basis of the Gaia quality flags. It has indeed been shown that the 2nd Gaia data release is characterized by spatial variation of the astrometric accuracy occurring at both small and large scales (from a few arcminutes to several degrees) with a patchy distribution across the sky, depending on the local stellar density and the satellite scanning law (Arenou et al. 2018). So, any cut made on the basis of astrometric quality parameters would spuriously decrease the stellar density of the less surveyed regions. On the other hand, the inclusion of stars with poorly measured astrometric/photometric parameters increases the noise in the density determination, so that the cost-effectiveness of the application of quality cuts is not trivial to be assessed. As a test, I compared the density maps of the GC NGC 5139, where tidal tails were already detected using the same dataset adopted here (Ibata, et al. 2019a), derived with and without the application of various cuts in parallax/proper motion errors: the inclusion of quality cuts, while requiring a fine tuning to avoid the emergence of patches parallel to the Gaia scanning law, produces no significant improvement in the detection of tidal tails. So, the only selection applied to the catalog has been made on the basis of the dereddened G magnitude. Indeed, for the reliability of the present analysis, it is crucial to ensure a

constant source detection efficiency across the analysed field of view, and the completeness fluctuations of Gaia at its faint end can significantly affect the results of the analysis. The adopted magnitude cut (G_{cut}) varies from cluster to cluster and has been set to ensure a smooth variation of the density across the analysed field of view. For this purpose, the following procedure has been adopted:

- For different guesses of G_{cut} , the sources with $|G - G_{cut}| < 0.25$ have been selected;
- The field of view has been divided in $6' \times 6'$ bins evenly distributed within an annulus with internal and external radii of 1° and 5° around the cluster centre, and the number of selected sources contained in each bin has been counted;
- The logarithm of star counts has been fitted by a first order polynomial in $(X, Y, \log N)$ and the r.m.s of the fit has been calculated;
- The largest value of G_{cut} ensuring a *r.m.s.* $< 0.05 dex$ has been adopted.

The values of G_{cut} determined according to the above procedure lie in the range $20 < G_{cut} < 21$, with brighter cuts in those GCs located in densely populated regions (i.e. close to the Galactic plane and/or the bulge) or characterised by a small number of Gaia passages.

Corrected distances (X, Y) and proper motions have been calculated using an orthographic projection of the canonical celestial coordinates and proper motions (see eq. 2 of Gaia Collaboration, et al. 2018b).

3 METHOD

The algorithm adopted in this work is a 5D mixture modelling (McLachlan & Basford 1988). Schematically, the distribution of a representative sample of cluster members and Galactic field stars in the parameter space is modelled with suitable analytic functions. The relative normalization of the model cluster and field distributions is calculated through a maximum-likelihood technique using samples of stars located in different region of the analysed field and used to determine the local density of cluster stars.

The stars contained within (outside) $\Delta R < 0.5^\circ$ from the cluster centre (from Goldsbury, Heyl & Richer 2013), $\Delta\mu < 2 \text{ mas yr}^{-1}$ from the systemic cluster motion (from Baumgardt, et al. 2019)² and $\Delta p < 5\epsilon_p$ from the measured cluster parallax (from Gaia Collaboration, et al. 2018b, ; where ϵ_p is the parallax error) have been selected as *reference samples* for the cluster (field) population.

The parallax distribution of cluster stars has been assumed to be a Dirac delta centered on the mean cluster parallax. This is a reasonable assumption since the parallax differences among cluster stars are more than 100 times smaller than the typical parallax uncertainty in all the GCs of the sample. So, the probability ($P_{p,i}^c$) for a star to be a cluster member, on the basis of its parallax only, is given by

$$\ln P_{p,i}^c = -\frac{(p_i - \langle p \rangle_c)^2}{2 \epsilon_{p,i}^2} - \ln(\epsilon_{p,i}) \quad (1)$$

¹ Although the reddening maps of Lallement et al. (2019) are calculated using only stars up to 3 kpc from the Sun, at Galactic latitudes $|b| > 10^\circ$ they include more than 99.9% of the dust column density along the line of sight of all the GCs analysed in this work.

² for NGC5139, because of its large extent and velocity dispersion, these conditions have been set to $\Delta R < 0.8^\circ$ and $\Delta\mu < 2.3 \text{ mas yr}^{-1}$

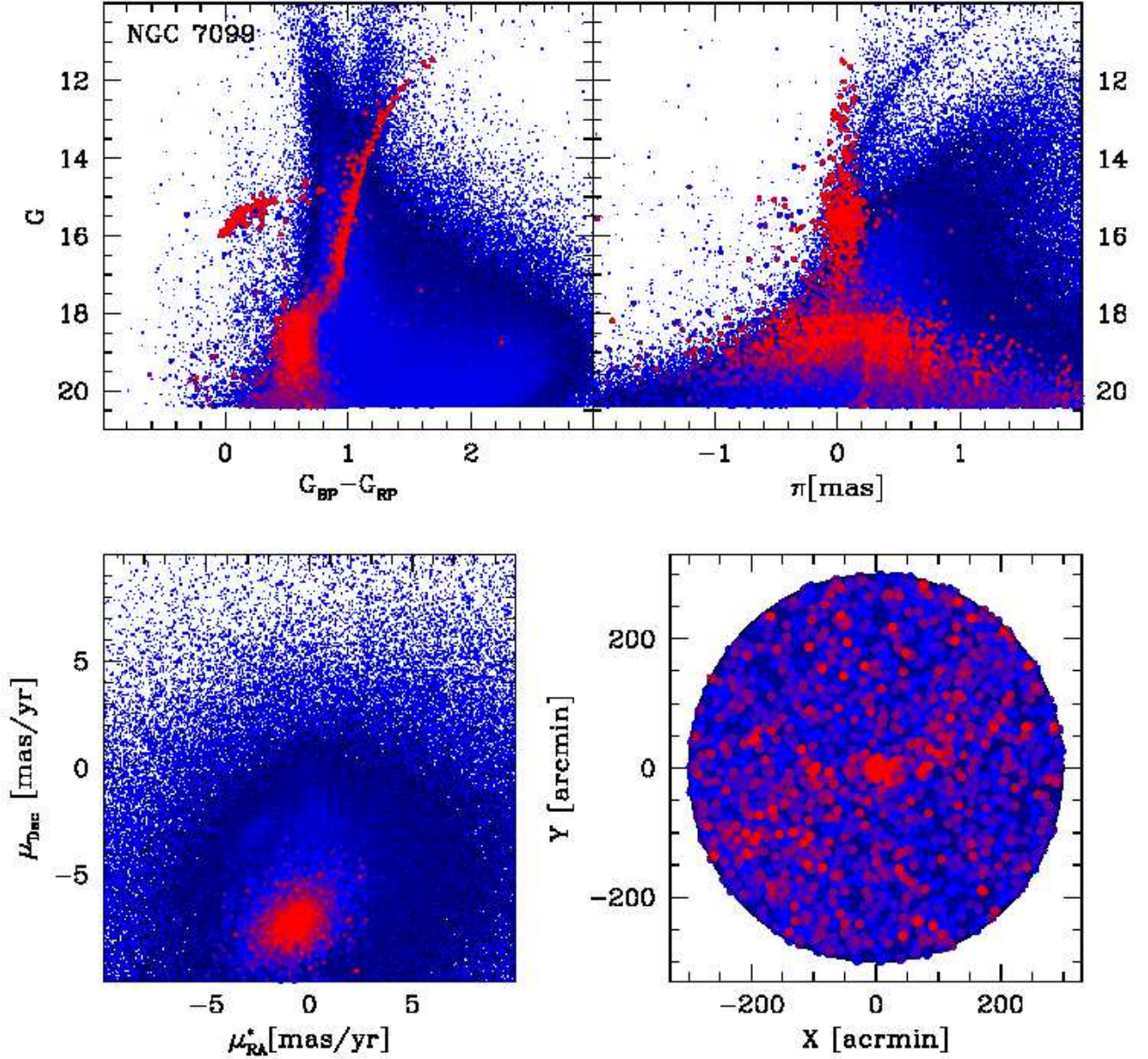


Figure 1. Distribution of NGC 7099 stars in several planes of the parameter space. Top-left: $G_{BP} - G_{RP}, G$ colour-magnitude diagram; top-right: parallax- G magnitude plane; Bottom-left: proper motions plane; Bottom-right: projected positions map. Stars with increasing cluster-to-field probability contrast $\Delta \ln P$ are plotted with colours from blue to red (grey to black in the printed version of the paper).

where p_i and $\epsilon_{p,i}$ are the parallax of the i -th star and its associated uncertainty and $\langle p \rangle_c$ is the mean cluster parallax in units of mas . The distribution of field star parallaxes has been fitted with the empirical function

$$\Gamma(p) = \left(1 + \frac{p}{a_1}\right)^{-\alpha_1} \left(1 + \frac{p}{a_2}\right)^{-\alpha_2} \quad (2)$$

The best fit values of a_1 , a_2 , α_1 and α_2 have been determined using a Monte Carlo scheme. For any guess of the a_1 , a_2 , α_1 and α_2 parameters, N_f (equal to the number of *reference sample* field stars) synthetic parallaxes have been ran-

domly extracted from the corresponding $\Gamma(p)$ distribution (eq. 2). Real and synthetic star parallaxes have been sorted and a gaussian shift with dispersion equal to the parallax uncertainty of each star has been added to the corresponding particle. The cumulative distributions of real and synthetic parallaxes have been then compared using a Kolmogorov-Smirnov test and the values of the parameters providing the largest KS probability have been chosen. The probability for a star to be a field star, on the basis of its parallax, is given

by

$$\ln P_{p,i}^f = \ln \int_0^{+\infty} \Gamma(p) \exp \left[\frac{-(p-p_i)^2}{2\epsilon_{p,i}^2} \right] dp - \ln \left(\sqrt{2\pi}\epsilon_{p,i} \int_0^{+\infty} \Gamma(p) dp \right) \quad (3)$$

The distribution of cluster stars in the proper motions space has been modelled with a 2D Gaussian with a decreasing dispersion as a function of distance from the cluster centre according to the prediction of the King (1966) model best fit of de Boer, et al. (2019). The normalization of the model proper motion dispersion profile has been chosen by maximising the log-likelihood

$$\begin{aligned} \ln L &= \sum_{i=1}^N \ln P_{\mu,i} \\ \ln P_{\mu,i} &= -\frac{1}{2} [\delta X_i^2 + \delta Y_i^2 - 2\tilde{\rho}_i \delta X_i \delta Y_i + \ln(1 - \tilde{\rho}_i^2) + \ln(s_{\mu X,i}^2 s_{\mu Y,i}^2)] - \ln(2\pi) \end{aligned} \quad (4)$$

where

$$\begin{aligned} \delta X_i^2 &= \frac{(\mu_{\alpha,i}^* - \langle \mu_{\alpha}^* \rangle_c)^2}{(1 - \tilde{\rho}_i^2) s_{\mu X,i}^2} \\ \delta Y_i^2 &= \frac{(\mu_{\delta,i} - \langle \mu_{\delta} \rangle_c)^2}{(1 - \tilde{\rho}_i^2) s_{\mu Y,i}^2} \\ s_{\mu X,i}^2 &= \epsilon_{\mu\alpha,i}^2 + \sigma^2(R_i) \\ s_{\mu Y,i}^2 &= \epsilon_{\mu\delta,i}^2 + \sigma^2(R_i) \\ \tilde{\rho}_i &= \frac{\rho_i \epsilon_{\mu\alpha,i} \epsilon_{\mu\delta,i}}{s_{\mu X,i} s_{\mu Y,i}} \end{aligned} \quad (5)$$

among the $N = N_c$ *reference sample* cluster stars. In the above equations, $\langle \mu_{\alpha}^* \rangle_c$ and $\langle \mu_{\delta} \rangle_c$ are the systemic cluster proper motions, $\mu_{\alpha,i}^*$ and $\mu_{\delta,i}$ are the proper motions of the i -th star, $\epsilon_{\mu\alpha,i}$, $\epsilon_{\mu\delta,i}$ are the proper motion errors, ρ_i is the correlation coefficient of the two uncertainties and $\sigma(R_i)$ is the normalised model proper motion dispersion at the projected distance of the i -th star (in units of $mas\ yr^{-1}$). For the field population, the proper motion distribution has been modelled with a 2D tilted gaussian function with parallax-dependent dispersion

$$\sigma(p) = \frac{a}{p} \{1 + \exp[b(\log p - c)]\} \quad (6)$$

The values of the free parameters a , b , c and θ have been derived by maximising the log-likelihood of eq. 4 applied to the *reference sample* field stars ($N = N_f$) and using

$$\begin{aligned} \delta X_i^2 &= \frac{[(\mu_{\alpha,i}^* - \langle \mu_{\alpha}^* \rangle_f) \cos \theta + (\mu_{\delta,i} - \langle \mu_{\delta} \rangle_f) \sin \theta]^2}{(1 - \tilde{\rho}_i^2)(s_{X,i}^2 + \sigma^2(p_i))} \\ \delta Y_i^2 &= \frac{[-(\mu_{\alpha,i}^* - \langle \mu_{\alpha}^* \rangle_f) \sin \theta + (\mu_{\delta,i} - \langle \mu_{\delta} \rangle_f) \cos \theta]^2}{(1 - \tilde{\rho}_i^2)(s_{Y,i}^2 + \sigma^2(p_i))} \\ s_{X,i}^2 &= \epsilon_{\mu\alpha,i}^2 \cos^2 \theta + \epsilon_{\mu\delta,i}^2 \sin^2 \theta + \rho_i \sin 2\theta \epsilon_{\mu\alpha,i} \epsilon_{\mu\delta,i} \\ s_{Y,i}^2 &= \epsilon_{\mu\alpha,i}^2 \sin^2 \theta + \epsilon_{\mu\delta,i}^2 \cos^2 \theta - \rho_i \sin 2\theta \epsilon_{\mu\alpha,i} \epsilon_{\mu\delta,i} \\ \tilde{\rho}_i &= \frac{(s_{Y,i}^2 - s_{X,i}^2) \sin 2\theta + 2(\rho_i s_{X,i} s_{Y,i} \cos 2\theta)}{2\sqrt{(s_{X,i}^2 + \sigma^2(p_i))(s_{Y,i}^2 + \sigma^2(p_i))}} \end{aligned} \quad (7)$$

where $\langle \mu_{\alpha}^* \rangle_f$ and $\langle \mu_{\delta} \rangle_f$ are the mean systemic proper motion of *reference* field stars in the two directions³.

The density of *reference sample* cluster stars at the position of the i -th star in the $(G_{BP} - G_{RP})$, G colour-magnitude diagram (Λ_{CMD}^c) has been calculated using a k -nearest neighbour algorithm (with $k=10$) and assuming a metric between colours and magnitudes $(\Delta_{G_{BP}-G_{RP}}, \Delta_G) = (1, 6)$ i.e. corresponding to the average ratio of standard deviations in colours and magnitudes of *reference sample* cluster stars in the considered sample of GCs.

$$\Lambda_{CMD,i} = \frac{10}{\pi \left[\Delta_{G_{BP}-G_{RP}}^2 + \left(\frac{\Delta_G}{6} \right)^2 \right]}$$

where $\Delta_{G_{BP}-G_{RP}}$ and Δ_G are the colour and magnitude difference between the i -th star and its 10-th nearest neighbour. The corresponding cluster membership probability is given by

$$\ln P_{CMD,i}^c = \ln \Lambda_{CMD,i}^c - \ln N_c \quad (8)$$

The field probability has been calculated using same algorithm applied to the *reference sample* of field stars with $\Delta \log p < 0.1$ from the considered star

$$\ln P_{CMD,i}^f = \ln \Lambda_{CMD,i}^f - \ln N_{f,i} \quad (9)$$

where $N_{f,i}$ is the number of *reference sample* field stars contained in the interval encompassing the parallax of the i -th star⁴.

The total membership probability to the cluster (field) population has been obtained from eqs 1, 4, 5 and 8 (and 3, 4, 7, 9, respectively) as

$$\begin{aligned} \ln P_i^c &= \ln P_{p,i}^c + \ln P_{\mu,i}^c + \ln P_{CMD,i}^c \\ \ln P_i^f &= \ln P_{p,i}^f + \ln P_{\mu,i}^f + \ln P_{CMD,i}^f \end{aligned}$$

Stars with a larger difference $\Delta \ln P \equiv \ln P^c - \ln P^f$ are those lying in a region of the parameter space with a larger contrast between cluster and field distributions (see Fig. 1).

The probabilities of stars located in different regions of

³ Note that the simplified functional forms of the parallax (eq. 2) and proper motion (eq. 6) distribution of field stars were chosen to adequately fit the observed distribution of *reference* field stars without adding a large number of free parameters. This choice is justified by the fact that, while a proper modelling of these distributions would require to account for the projection of the density and velocity ellipsoids of the various Galactic components along the various line of sights, as well as the Gaia selection function, the small-scale variations of such distributions are smoothed by the relatively large observational errors.

⁴ It should be noted that, at odds with the parallax and proper motion probabilities calculated convolving intrinsic distributions with individual uncertainties, the probability linked to the position in the CMDs includes the global effect of photometric uncertainties neglecting individual differences (i.e. I assigned the same probability to all stars lying in the same portion of the CMD, regardless of their individual colour/magnitude uncertainties). Again, this approximation is made to avoid a complex modelling of the intrinsic distribution in the colour-magnitude-parallax space which depends on many uncertain parameters (like star formation history, mass function, photometric completeness, mass-segregation, etc.).

the analysed field of view have been then used to derive the relative fraction of cluster-to-field stars. For this purpose, a grid with knots separated by $6'$ in both directions has been defined and stars contained within a projected distance R_{lim} from each knot have been selected. In two cases (NGC5272 and NGC5904) a nearby GC is present within the field of view (NGC5466 and Pal 5, respectively). For these cases, the area surrounding the nearby clusters has been masked (see Fig. 2 and 3). In each subsample of stars, the cluster-to-field ratio (η) has been chosen as the one maximizing the likelihood

$$\ln L = \sum_{i=1}^{N_{xy}} \eta \ln P_i^c + (1 - \eta) \ln P_i^f$$

and the corresponding density of cluster members is given by

$$\Sigma(X, Y) = \frac{\eta N_{xy}}{A(R_{lim})} \quad (10)$$

where N_{xy} and $A(R_{lim})$ are the number of stars in the subsample and its corresponding area.

The choice of R_{lim} should be adaptive to ensure a better resolution in regions with a large number of cluster members and a large smoothing in poorly populated regions. I adopted in each knot of the grid the minimum value of R_{lim} providing $\eta N_{xy} > 100$.

The above procedure should in principle provide a background-subtracted density map. On the other hand, an implicit assumption is that the adopted distribution of field stars in the parameter space does not vary within the field of view. While this is a reasonable assumption in many GCs of the sample, in GCs located in regions characterised by steep variation of the field population properties (i.e. those at low Galactic latitudes and/or close to the bulge) this approximation leads to a gradient in the derived density. However, given the relatively small size of the considered field of view, such a gradient has a small amplitude and varies smoothly across the field of view. For this purpose, the logarithm of the 2D density of regions at distances $R > 2^\circ$ from the cluster centre has been fitted with a first-order polynomial in the $(X, Y, \log \Sigma)$ space and subtracted.

The significance of the derived density has been estimated using a Monte Carlo technique. A sample of 10^3 extractions has been made by randomly reshuffling the position angles of all sources and calculating the corresponding density map. The r.m.s. of the various density determinations at distances $R > 2^\circ$ from the cluster centre has been adopted as the typical uncertainty.

4 RESULTS

4.1 Density maps

The projected density maps for the 18 GCs of the sample are shown in Figs 2 and 3. It is apparent that, while the density contours near the cluster centres are extremely regular, at large distances many clusters show anisotropic density distributions.

None of the previous works on this subject defined a rigorous criterion to claim the detection of tidal tails. Following the definition of tidal tails as "a collimated overdensity of stars emerging from the cluster in opposite directions"

(Toomre & Toomre 1972) I defined the two following criteria:

- The closed iso-density contour at 3σ above the background density containing the cluster centre must exceed a distance of 1.5 times the orbit-averaged Jacobi radius;
- The integrated projected density measured in opposite sectors must be significantly larger than that measured in the complementary region of the sky outside the Jacobi radius.

The first criterion implies the presence of the cluster population outside the Roche lobe. The orbit-averaged Jacobi radius (R_J) has been calculated by averaging over the orbit the Jacobi radius estimated using eq. A2 of Allen, Moreno & Pichardo (2006) and the GC masses by Baumgardt, et al. (2019). The cluster orbit has been integrated within the Galactic potential of Johnston, Spergel & Hernquist (1995) using a fourth-order Runge-Kutta integrator adopting the present-day systemic velocities listed by Baumgardt, et al. (2019).

The second criterion requires that the observed overdensity is preferentially oriented in one direction. For this purpose the annulus between R_J and $2R_J$ has been divided in two complementary regions constituted by opposite sectors of 90° width centered at a given position angle (see Fig. 5 of Sollima, et al. 2011). For each position angle, the ratio between the densities (measured using eq. 10) within each region has been calculated, and the position angle providing the maximum ratio (\mathcal{R}_{max}) has been chosen. The same estimate has been made in the Monte Carlo randomized extractions (see Sect. 3) and compared with \mathcal{R}_{max} . The alignment is considered statistically significant if \mathcal{R}_{max} is found to be larger than the same value measured in at least 997 (out 1000) Monte Carlo extractions.

Seven GCs pass the above criteria: NGC288, NGC2298, NGC5139, NGC5904, NGC6341, NGC6362 and NGC7099. Other GCs (like NGC3201 and NGC6752) show hint of tidal deformation at a low ($\sim 2\sigma$) significance level. Note that, among the 7 GCs with positive detection, in 5 cases (NGC288, NGC2298, NGC5139, NGC6341 and NGC7099) the tidal tails extend up to the border of the analysed field of view (at 5° from the cluster centre) and in two cases (NGC5139 and NGC7099) they remain significant at both sides of the cluster covering an extent of $\sim 10^\circ$.

It is also interesting to note that 4 (out 7) GCs show asymmetric tidal tails. Such an effect is expected in GCs close to their apo/peri-centres: in this situation, the velocity of stars varies quickly with the orbital phase so that stars in the leading (trailing) tail move away from the cluster while those in the trailing (leading) tail slowly approach the cluster when it leaves (reaches) the extreme of the orbit. However, while all the 4 GCs exhibiting asymmetric tails are relatively close to their apo/peri-centers, in only 2 of them the observed elongation is directed toward the expected direction. So, a more likely explanation is that this evidence is due to statistical fluctuations occurring close to the threshold density which make appear only one side of the tails.

4.2 Comparison with literature works

The GCs analysed in this work have been already studied in the past using different photometric datasets. In partic-

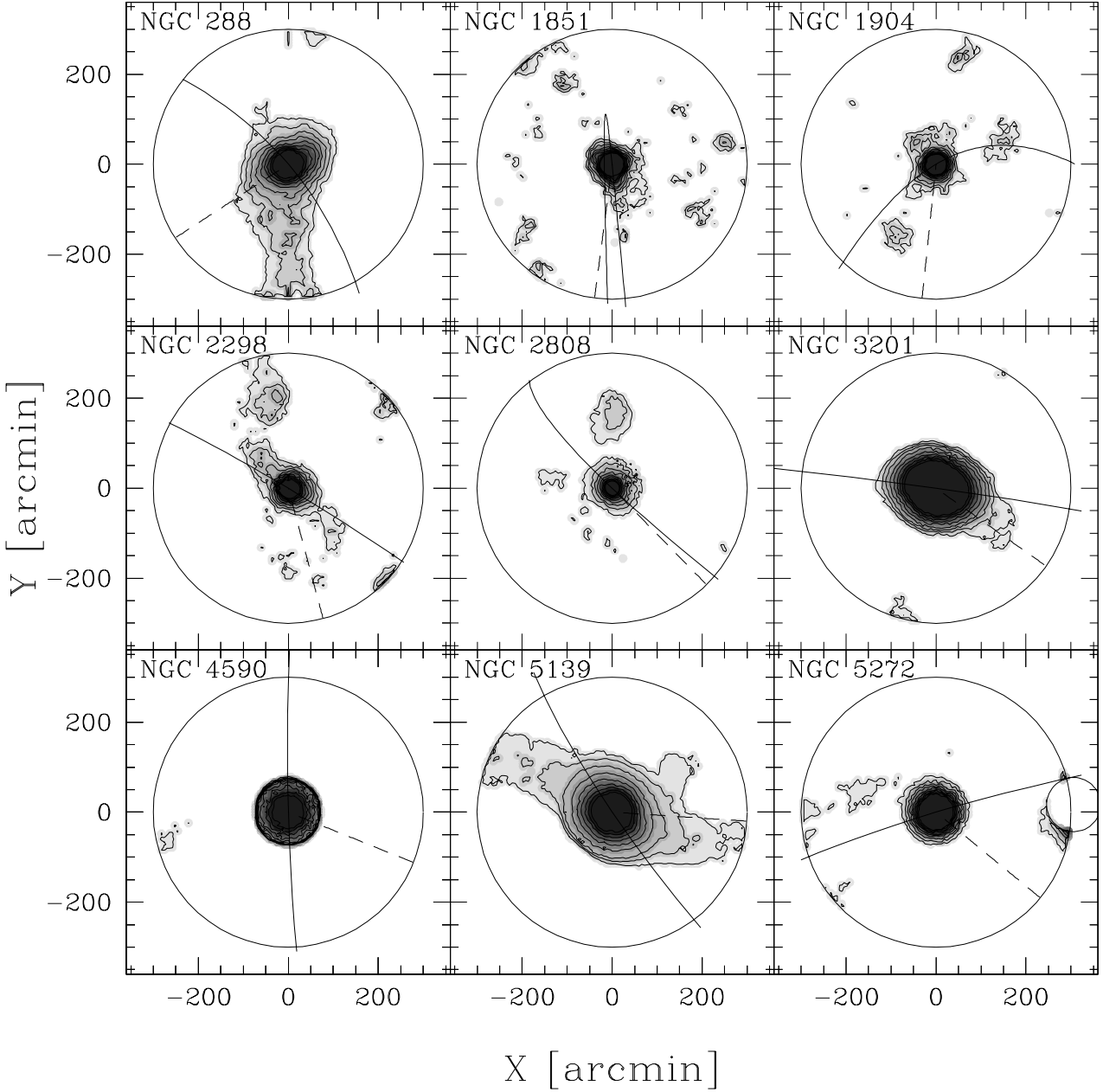


Figure 2. Projected density map for the GCs NGC288, NGC1851, NGC1904, NGC2298, NGC2808, NGC3201, NGC4590, NGC5139 and NGC5272. Contours from 2 to 10σ above the background density are plotted in logarithmic scale in steps of 1σ . The cluster orbital path and the direction to the Galactic centre are overlotted as solid and dashed lines, respectively.

ular, the tidal tails of NGC 288 have been discovered up to the same distance from the cluster centre and with the same orientation found in the present study by Shipp, et al. (2018) using photometric data from the Dark Energy Survey, and Kaderali, et al. (2019) using Gaia data. Previous studies (Grillmair, et al. 1995; Leon, Meylan & Combes 2000; Piatti 2018) also found low-significance distortion close to the tidal radius of this cluster.

Ibata, et al. (2019a) used Gaia data to detect the same tidal feature observed here around NGC5139, which appears to be extended for $\sim 28^\circ$ and connected with the previously

discovered Fimbulthul stream (Ibata, Malhan & Martin 2019b). The detection of tidal tails around NGC5139 was also claimed by Leon, Meylan & Combes (2000) but questioned by Law, et al. (2003) because of the effect of differential reddening neglected by the former study.

Similarly, Grillmair (2019) found a $\sim 50^\circ$ -extended tidal tails around NGC5904 using Gaia data selected over and area > 6000 sq.deg. Also in this case, small tidal distortions in NGC5904 were previously reported by Leon, Meylan & Combes (2000) and Jordi & Grebel (2010).

Some density excess close to the tidal radii of NGC2298

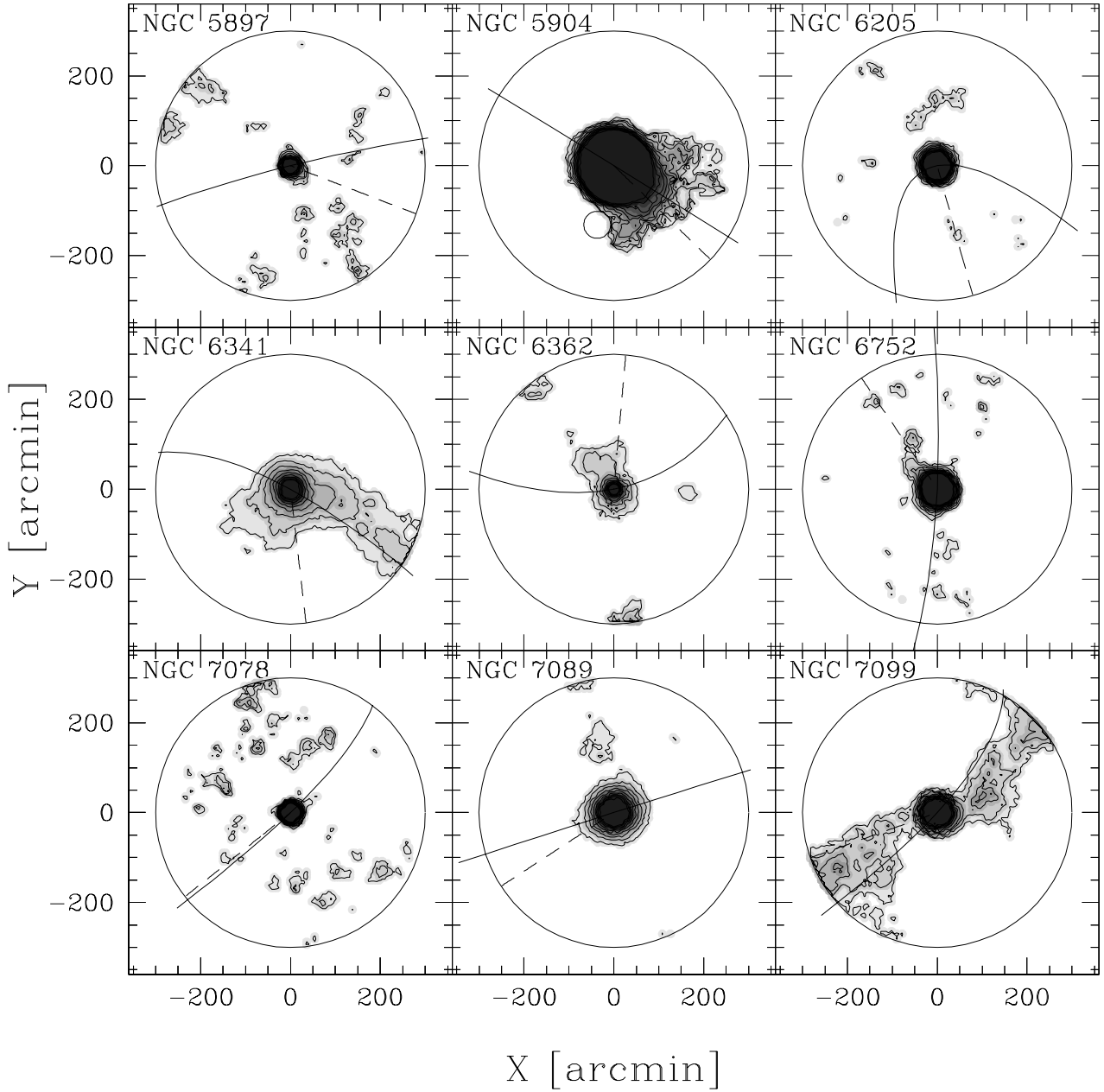


Figure 3. Same as Fig. 2 for NGC5897, NGC5904, NGC6205, NGC6341, NGC6362, NGC6752, NGC7078, NGC7089 and NGC7099.

(Leon, Meylan & Combes 2000; Balbinot, et al. 2011; Carballo-Bello, et al. 2018) and NGC7099 (Chun, et al. 2010) have been reported in the past. However, none of them reach a comparable level of significance and extent with respect to that found in the present work.

No previous studies have found any extra-tidal feature around NGC6362 and NGC6341.

Among the other GCs analysed here, low-amplitude overdensities outside the tidal radii have been claimed in NGC1851 (Leon, Meylan & Combes 2000; Carballo-Bello, et al. 2018; Shipp, et al. 2018), NGC1904 (Grillmair, et al. 1995; Leon, Meylan & Combes

2000; Carballo-Bello, et al. 2018; Shipp, et al. 2018), NGC2808 (Grillmair, et al. 1995; Chen & Chen 2010; Carballo-Bello, et al. 2018), NGC3201 (Grillmair, et al. 1995; Chen & Chen 2010; Bianchini, Ibata & Famaey 2019), NGC4590 (Grillmair, et al. 1995), NGC5272 (Leon, Meylan & Combes 2000), NGC6205 (Leon, Meylan & Combes 2000), NGC7008 (Grillmair, et al. 1995; Jordi & Grebel 2010; Chun, et al. 2010) and NGC7089 (Grillmair, et al. 1995). It is not easy to compare the results presented in this paper with those of the above studies, since all of them use different thresholds and smoothing levels and in most cases the identification

of extra-tidal features is made on the basis of a qualitative inspection of the density map. Consider also that the lack of detection in the present study of significant tidal tails around these GCs could be due to the limiting magnitude of Gaia ($20 < G_{cut} < 21$; see Sect. 2.2), significantly brighter than those of many of the above studies. This is particularly important in distant GCs where, in spite of the lack of astrometric information, their deep photometry allows to sample the cluster stellar population better by a factor of 10 or more, even in the intrinsically poorly populated periphery of GCs.

4.3 Tidal tails orientation

As introduced in Sect. 1, because of the different directions of the forces acting on stars within/close to the Jacobi radius and at large distance from the cluster centre, tidal tails are expected to show a characteristic S-shape, with the innermost part elongated toward the Galactic centre and a torsion toward the cluster orbital path at large distances (Montuori, et al. 2007; Klimentowski, et al. 2009).

Qualitatively, this prediction seems to be verified in many of the GCs showing extended overdensities outside their tidal radii (see Figs 2 and 3). In particular, the inner density contours of NGC288, NGC5139, NGC5904, NGC6362 and NGC7099 (and with a smaller significance also in NGC3201 and NGC6752) appear to be elongated in the direction of the Galactic centre. On the other hand, in NGC288, NGC6341 and NGC7099, where it is possible to detect the tidal tails up to several degrees, the orientation of the overdensity tends to rotate toward the cluster orbital path.

To quantitatively test the above hypothesis, in the 5 GCs showing the most extended extra-tidal overdensities (NGC288, NGC2298, NGC5139, NGC6341 and NGC7099), the field of view outside $0.5 R_J$ has been divided in annuli of 0.1° width and the background-subtracted density of each annulus as a function of the position angle has been fitted with a cosine function. The angle corresponding to the phase of maximum of the best fit curve is plotted as a function of the distance from the centre of each of the 5 considered GCs in Fig. 4. In all cases, the observed orientation is located in the portion of the plane contained between the direction of the orbit and that of the Galactic centre. In NGC288 and NGC7099 a drift of the tidal tails position angle from the direction of the Galactic centre to that of the cluster orbit at increasing distances is noticeable.

A χ^2 test applied to regions at $R > R_J$ in each individual GC indicates probabilities $66\% < P_{\chi^2} < 86\%$ that the distribution of position angles follows the same trend of the orbit⁵. On the other hand, if all the 5 GCs are considered together, the same test gives a probability of 99.8%, indicating a significant general alignment of the outer portion of the tails with the orbital paths in this sample of GCs.

4.4 Destruction rates

The stars contained in the tidal tails have been lost in recent epochs by the GCs. Although, after its expulsion, the distance of a star from the cluster centre follows a non-monotonic variation with time according to the eccentricity of the cluster orbit (Küpper, et al. 2010; Küpper, Lane & Heggie 2012), the phase delay of groups of stars evaporated at different epochs increases with time, so that stars in the tails at increasing distance from the centre were on average expelled at earlier epochs. It is therefore possible to link the fraction of stars contained in the tidal tails with the rate at which a cluster loses its mass through a comparison with suitable models.

For this purpose, as a first step I calculated the number of stars contained in the tidal tails (N_{obs}^{tails}) and within the cluster tidal radius (N_{obs}^{in}) in the 5 GCs with the most prominent tidal tails (NGC288, NGC2298, NGC5139, NGC6341 and NGC7099). The first quantity has been calculated by integrating the background-subtracted projected density within two 60° -wide regions located at the opposite sides of each cluster at distances $R > 1.5 R_J$ encompassing the tidal tails (see Fig. 5). Unfortunately, the same approach cannot be adopted in the cluster central region characterised by high stellar density and consequently low completeness. So, the number of stars inside the cluster has been estimated by normalizing the projected density profile of the King (1966) model best fit of de Boer, et al. (2019) to the density measured in the outer portion of the cluster, which should not be affected by significant crowding. The total number of stars has been then calculated by integrating the model profile from the center to R_J .

The mass-loss history of each GC has been modelled using the technique of streaklines (Küpper, Lane & Heggie 2012). Briefly, the orbit of each cluster has been reconstructed and, at each integration step, a particle with a small ($\Delta E < 0.1 \text{ km}^2 \text{ s}^{-2}$) positive energy has been put at one of the Lagrangian points and with a velocity directed outward from the cluster. The orbit of each ejected particle and that of the GC (simulated as a point mass particle) have been then followed together within the Galactic potential for 2 Gyr till the present-day position of the cluster. I neglected the cluster mass variation since stars in the portion of the tails analysed here are those ejected at recent epochs in a short time interval (from 0.12 to 1 Gyr depending on the cluster orbit), during which the clusters lost a small ($< 6\%$ in all cases) of their present-day mass. This approach is faster than a canonical N-body simulation (since the orbit of the escaped stars are followed individually neglecting mutual interactions and with the relatively long timestep required to accurately integrate their orbit), and has been proven to be effective in reproducing the structure and evolution of tidal tails (Küpper, Lane & Heggie 2012; Mastrobuono-Battisti, et al. 2012). As already assumed in Sect. 4.1, the cluster orbits have been integrated within the Johnston, Spiegel & Hernquist (1995) Galactic potential, using the cluster masses and present-day positions and velocities of Baumgardt, et al. (2019). The (constant) mass-loss rate of each simulation has been set to $10^4 \text{ stars Gyr}^{-1}$,

⁵ For this test, the averages between the leading and trailing directions of the orbit have been used.

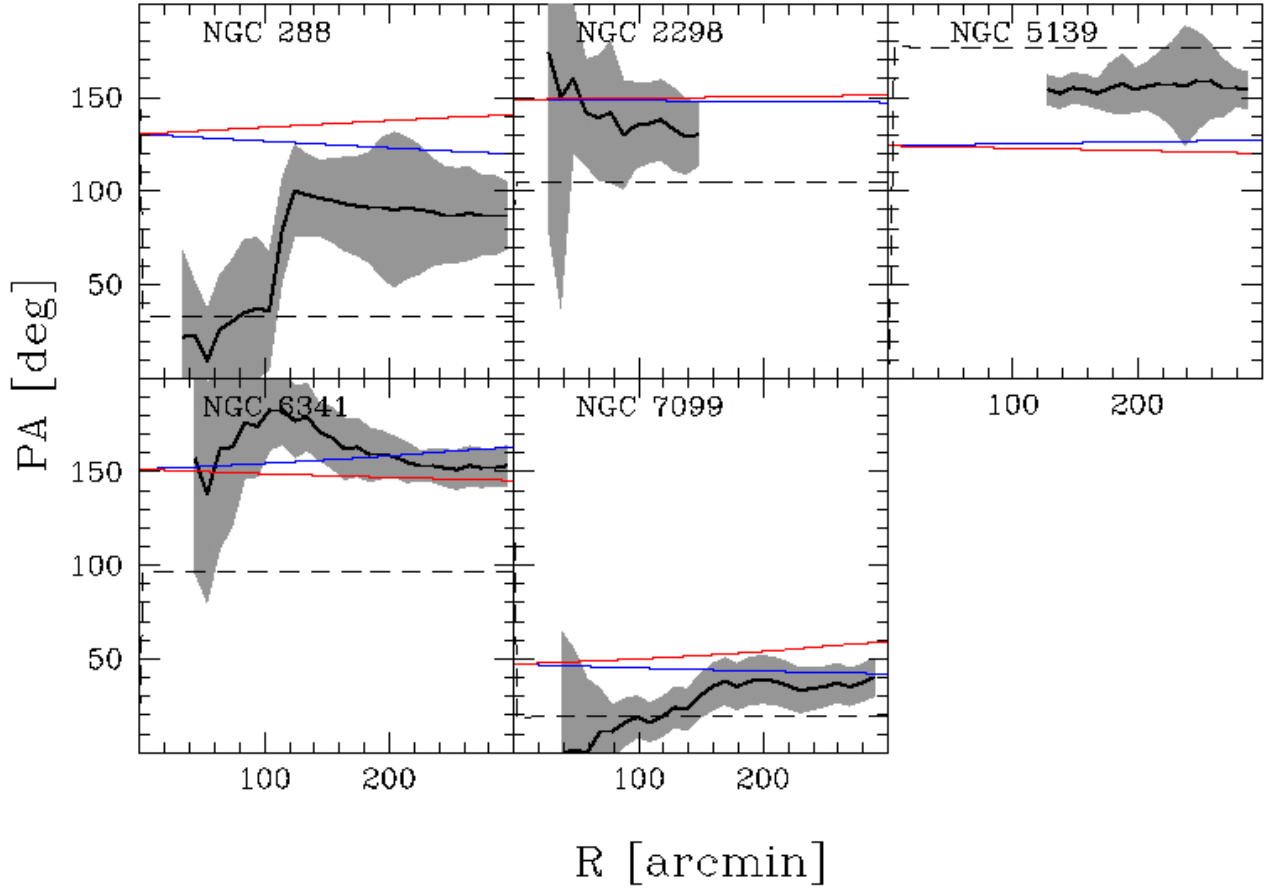


Figure 4. Position angle of the tidal tails as a function of the projected distance from the cluster centre (black solid lines) for NGC288, NGC2298, NGC5139, NGC6341 and NGC7099. The shaded area mark the 1σ uncertainty. The direction of the leading (blue lines; dotted lines in the printed version of the paper) and trailing (red lines; dot-dashed lines in the printed version of the paper) sides of the orbit and that to the Galactic centre (black dashed lines) are overlotted.

which ensures to simulate a statistically significant number of tidal tails stars in a reasonable computation time. At the end of the simulation, the positions and velocities of simulated particles have been converted into equatorial coordinates, proper motions and radial velocities. The particles with proper motions within $\Delta\mu < 2 \text{ mas yr}^{-1}$ from the systemic cluster motion and contained within the same regions defined above for observations, have been counted providing the number of predicted stars in tidal tails (N_{sim}^{tails}) for the assumed mass-loss rate.

The fractions of mass lost per unit time (the so-called “destruction rate”) have been therefore calculated as

$$\nu = \frac{10^4 N_{obs}^{tail}}{N_{obs}^{in} N_{sim}^{tails}}$$

and are listed in Table 1.

Of course, many approximations are made in the above estimate: real clusters lose stars non-uniformly during their evolution, and the evolution of the cluster and Galactic potentials are neglected. More importantly, two-body relaxation lead to a preferential loss of low-mass stars, so that the mass function of in the tails is expected to be significantly different from that within the cluster tidal ra-

dius (Balbinot & Gieles 2018). So, the estimated mass-loss rates are lower limits to the actual values. In this context, two-body relaxation proceeds in each cluster on different timescales, so that this effect can affect different clusters in different ways. However, the mass range sampled by Gaia is relatively small ($0.6 < M/M_{\odot} < 0.8$) and similar in all the considered GCs, so this effect should affect the above estimate only at a second order.

The derived destruction rates range between $0.018 < \nu/Gyr^{-1} < 0.085$, corresponding to dissolution times between 12 and 55 Gyr. The destruction rates derived here agree with the predictions calculated for the same GCs of Gnedin & Ostriker (1997) (using Fokker-Planck simulations) and direct N-body simulations (H. Baumgardt; private communication), while they are significantly larger than those reported by Allen, Moreno & Pichardo (2006). It should be considered that all these theoretical works adopt different Galactic potentials, cluster orbits and filling factors, so a detailed comparison is not possible.

According to a large number of studies (Gnedin & Ostriker 1997; Balbinot & Gieles 2018) based on theoretical arguments and simulations, the mass loss rate of a star cluster is determined by the combination of internal

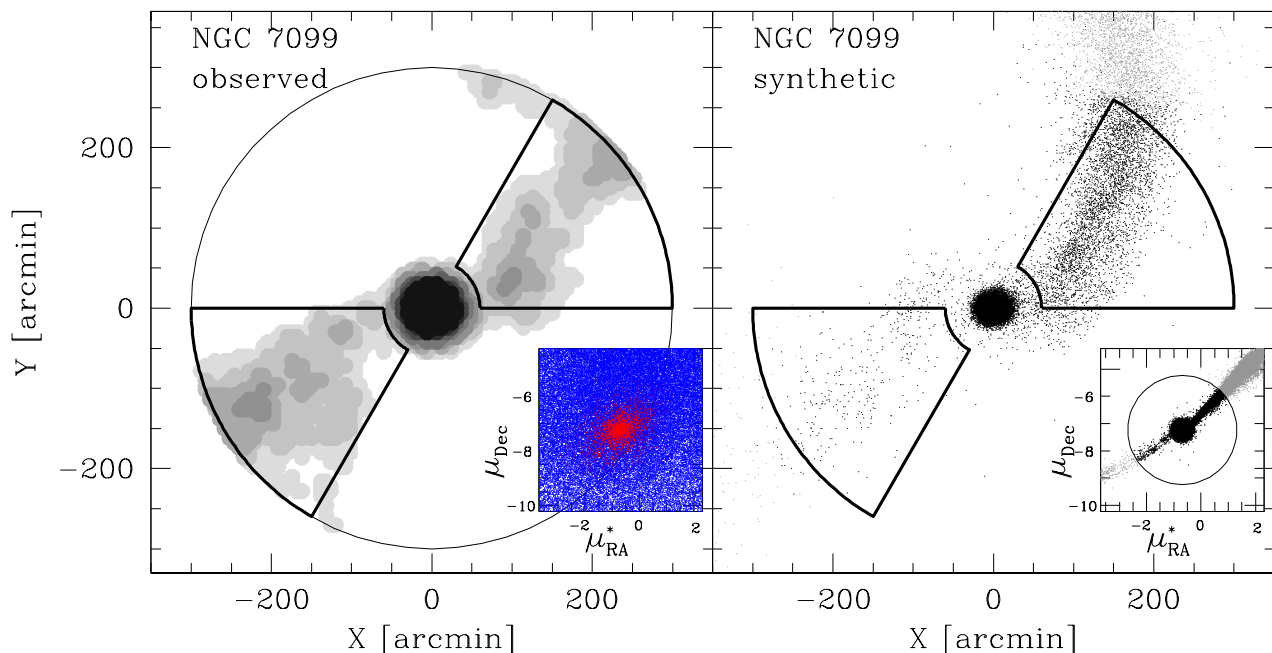


Figure 5. Left panel: observed density map of NGC7099. The proper motion probability contrast map is plotted in the inset using the same colour code of Fig. 1. Right panel: projected distribution of synthetic particles of the corresponding simulation. The proper motion distribution is shown in the inset. Black and grey dots correspond to particles within and outside the proper motion selection box. The adopted selection boxes are overlotted to both panels as thick black lines.

(due to two-body relaxation) and external (due to tidal shocks experienced during passages across the Galactic disk and at the peri-Galacticon) effects. The two above processes have different dependences on the cluster characteristics: the internal process is expected to produce an almost constant mass loss rate every half-mass relaxation time (Spitzer 1987), while the external process depends on the orbital characteristics (Ostriker, Spitzer & Chevalier 1972; Aguilar, Hut & Ostriker 1988). Unfortunately, because of the small number of GCs with significant tidal tails, it is not possible to perform a meaningful analysis of correlations with the parameters affecting the mass loss. However, at face value, the Pearson correlation coefficients between the logarithm of the destruction rate and those of the half-mass relaxation time (from Baumgardt, et al. 2019) and tidal shocks-related destruction rate (given by the sum of eq.s 1 and 2 of Dinescu, Girard & van Altena 1999) turn out to be -0.60 and 0.36, respectively. While the small sample size makes both correlations not significant, they are expected since in GCs with short relaxation times two-body relaxation has efficiently pushed the energy of their stars beyond the escape threshold, and GCs with strong tidal interactions are easily destroyed.

5 CONCLUSIONS

I reported the results of a comprehensive analysis of the projected density map of a sample of 18 Galactic GCs us-

ing the set of astrometric and photometric data provided by the Gaia 2nd data release. The use of all the available information in the 5D space composed by parallaxes, proper motions and magnitudes allowed to optimally separate the signal of the cluster population from the contamination from fore/background Galactic field interlopers. This allowed to sample the cluster population down to very faint surface brightness levels.

The derived maps show significant deviation from sphericity close to the tidal radii of many analysed GCs. For 7 (out of 18) GCs these overdensities are statistically significant up to distances exceeding the size of the Roche lobe being likely produced by the strain exerted by the Galactic tidal forces. In 5 GCs the detected overdensities extend up to several degrees from the cluster centre (extending over 10° in NGC5139 and NGC7099) and show the typical shape of symmetric tidal tails emerging from the cluster. While for a few GCs (NGC288, NGC5139, NGC5904) these features were already reported by previous studies (Shipp, et al. 2018; Ibata, et al. 2019a; Grillmair, et al. 1995), the other detections (in NGC2298, NGC6341, NGC6362, NGC7099) are new discoveries.

The orientation of the tails follows the predictions of dynamical models: in most of the GCs of the sample, the inner density contours are preferentially aligned with the direction of the Galactic center (i.e. the direction of the Galactic potential gradient) which determines the elongation of the Roche lobe. On the other hand, at large distances the GCs with the most extended features show tidal tails aligned with

the orbital path of the cluster. In spite of the uncertainties in the Galactic potential, GC distances and velocities, this last evidence is statistically significant when the whole set of GCs is considered. In principle, the morphology of the tidal tails could be used to constrain the shape of the Galactic potential (in particular its flattening and the halo-to-disk normalisation). However, for this task a larger sample of GCs with tidal tails extending over a wider area than that analysed here would be needed.

For the same set of 5 GCs, the fraction of stars contained in the tidal tails has been used to make the first observational estimate of the present-day mass-loss rate. Till now, these rates have been only predicted simulating the long-term evolution of satellites within a Galactic potential through numerical simulations or analytical prescriptions (Gnedin & Ostriker 1997; Dinescu, Girard & van Altena 1999; Allen, Moreno & Pichardo 2006). Instead, in this work the destruction rate is directly linked to the observed fraction of stars contained in the visible portion of the tails. Although this estimate is subject to the uncertainties in the amplitude of the low-surface brightness tails and in the normalisation of the cluster profile, and neglects many dynamical processes (like e.g. mass-segregation; Balbinot & Gieles 2018), it depends only weakly on the modelled orbit and it is linked to an observational feature. Although the small sample size does not allow to draw any firm conclusion, the correlation of the destruction rate with the half-mass relaxation time is stronger than that with the tidal shocks strength, suggesting a dominant role of internal over external dynamical evolution in these GCs. This scenario is in agreement with the evidence of a tight anticorrelation between the mass function slope and half-mass relaxation time observed in a sample of 29 GCs by Sollima & Baumgardt (2017), since dynamically evolved GCs would experience a strong mass loss which efficiently deplete the low-mass end of their mass-functions (Baumgardt & Makino 2003) while producing at the same time prominent tidal tails features. However, further studies based on larger statistical samples are needed to clarify the significance of the above correlations.

The exceptional efficiency of the algorithm presented here is mainly due to the increase of the dimensionality of the available parameter space provided by Gaia. Still, the limiting factor is the inhomogeneous sampling at faint magnitudes of this survey which forces the adoption of a cut at relatively bright magnitudes. The next Gaia data releases will increase the power of tidal features detection because of the foreseen reduced uncertainties and better spatial sampling.

ACKNOWLEDGMENTS

I warmly thank Michele Bellazzini for useful discussions and Holger Baumgardt for providing his unpublished destruction rates. I also thank the anonymous referee for his/her helpful comments and suggestions that improved my paper.

REFERENCES

Aguilar L., Hut P., Ostriker J. P., 1988, *ApJ*, 335, 720

- Allen C., Moreno E., Pichardo B., 2006, *ApJ*, 652, 1150
 Arenou F., et al., 2018, *A&A*, 616, A17
 Balbinot E., Santiago B. X., da Costa L. N., Makler M., Maia M. A. G., 2011, *MNRAS*, 416, 393
 Balbinot E., Gieles M., 2018, *MNRAS*, 474, 2479
 Baumgardt H., Makino J., 2003, *MNRAS*, 340, 227
 Baumgardt H., Hilker M., Sollima A., Bellini A., 2019, *MNRAS*, 482, 5138
 Belokurov V., et al., 2006a, *ApJL*, 642, L137
 Belokurov V., Evans N. W., Irwin M. J., Hewett P. C., Wilkinson M. I., 2006b, *ApJL*, 637, L29
 Bergond G., Leon S., Guibert J., 2001, *A&A*, 377, 462
 Bianchini P., Ibata R., Famaey B., 2019, *ApJL*, 887, L12
 Binney J., Tremaine S., 1987, in "Galactic Dynamics", David N. Spergel eds., Princeton NJ
 Bressan A., Marigo P., Girardi L., Salasnich B., Dal Cero C., Rubele S., Nanni A., 2012, *MNRAS*, 427, 127
 Carballo-Bello J. A., Martínez-Delgado D., Navarrete C., Catelan M., Muñoz R. R., Antoja T., Sollima A., 2018, *MNRAS*, 474, 683
 Carballo-Bello J. A., 2019, *MNRAS*, 486, 1667
 Casagrande L., Vandenberg D. A., 2018, *MNRAS*, 479, L102
 Chen C. W., Chen W. P., 2010, *ApJ*, 721, 1790
 Chun S.-H., et al., 2010, *AJ*, 139, 606
 Chun S.-H., Kang M., Jung D., Sohn Y.-J., 2015, *AJ*, 149, 29
 Dalessandro E., Miocchi P., Carraro G., Jílková L., Moitinho A., 2015, *MNRAS*, 449, 1811
 de Boer T. J. L., Gieles M., Balbinot E., Hénault-Brunet V., Sollima A., Watkins L. L., Claydon I., 2019, *MNRAS*, 485, 4906
 Dinescu D. I., Girard T. M., van Altena W. F., 1999, *AJ*, 117, 1792
 Duc P.-A., et al., 2015, *MNRAS*, 446, 120
 Erkal D., Koposov S. E., Belokurov V., 2017, *MNRAS*, 470, 60
 Fardal M. A., Babul A., Geehan J. J., Guhathakurta P., 2006, *MNRAS*, 366, 1012
 Fukushige T., Heggie D. C., 2000, *MNRAS*, 318, 753
 Gaia Collaboration, et al., 2018a, *A&A*, 616, A1
 Gaia Collaboration, et al., 2018b, *A&A*, 616, A12
 Gnedin O. Y., Ostriker J. P., 1997, *ApJ*, 474, 223
 Goldsbury R., Heyl J., Richer H., 2013, *ApJ*, 778, 57
 Grillmair C. J., Freeman K. C., Irwin M., Quinn P. J., 1995, *AJ*, 109, 2553
 Grillmair C. J., 2019, *ApJ*, 884, 174
 Harris W. E., 1996, *AJ*, 112, 1487
 Ibata R. A., Gilmore G., Irwin M. J., 1994, *Natur*, 370, 194
 Ibata R., Irwin M., Lewis G., Ferguson A. M. N., Tanvir N., 2001, *Natur*, 412, 49
 Ibata R. A., Bellazzini M., Malhan K., Martin N., Bianchini P., 2019a, *NatAs*, 3, 667
 Ibata R. A., Malhan K., Martin N. F., 2019b, *ApJ*, 872, 152
 Kaderali S., Hunt J. A. S., Webb J. J., Price-Jones N., Carlberg R., 2019, *MNRAS*, 484, L114
 King I. R., 1966, *AJ*, 71, 64
 Klimentowski J., Lokas E. L., Kazantzidis S., Mayer L., Mamon G. A., Prada F., 2009, *MNRAS*, 400, 2162
 Küpper A. H. W., Kroupa P., Baumgardt H., Heggie D. C., 2010, *MNRAS*, 401, 105
 Küpper A. H. W., Lane R. R., Heggie D. C., 2012, *MNRAS*, 420, 2700
 Johnston K. V., Spergel D. N., Hernquist L., 1995, *ApJ*, 451, 598
 Jordi K., Grebel E. K., 2010, *A&A*, 522, A71
 Lallement R., et al., 2019, *A&A*, 625, A135
 Law D. R., Majewski S. R., Skrutskie M. F., Carpenter J. M., Ayub H. F., 2003, *AJ*, 126, 1871
 Law D. R., Majewski S. R., 2010, *ApJ*, 714, 229
 Leon S., Meylan G., Combes F., 2000, *A&A*, 359, 907
 Lindegren L., et al., 2018, *A&A*, 616, A2

- Martínez-Delgado D., et al., 2010, *AJ*, 140, 962
- Mastrobuono-Battisti A., Di Matteo P., Montuori M., Haywood M., 2012, *A&A*, 546, L7
- McLachlan G. J., Basford K. E., 1988, in "Statistics: Textbooks and Monographs", Marcel Dekker eds., New York
- Montuori M., Capuzzo-Dolcetta R., Di Matteo P., Lepinette A., Mocchi P., 2007, *ApJ*, 659, 1212
- Myeong G. C., Jerjen H., Mackey D., Da Costa G. S., 2017, *ApJL*, 840, L25
- Navarrete C., Belokurov V., Kozlov S. E., 2017, *ApJL*, 841, L23
- Niederste-Ostholt M., Belokurov V., Evans N. W., Kozlov S., Gieles M., Irwin M. J., 2010, *MNRAS*, 408, L66
- Odenkirchen M., et al., 2001, *ApJL*, 548, L165
- Ostriker J. P., Spitzer L., Chevalier R. A., 1972, *ApJL*, 176, L51
- Piatti A. E., 2018, *MNRAS*, 473, 492
- Rockosi C. M., et al., 2002, *AJ*, 124, 349
- Röser S., Schilbach E., Goldman B., 2019, *A&A*, 621, L2
- Röser S., Schilbach E., 2019, *A&A*, 627, A4
- Shipp N., et al., 2018, *ApJ*, 862, 114
- Sollima A., Martínez-Delgado D., Valls-Gabaud D., Peñarrubia J., 2011, *ApJ*, 726, 47
- Sollima A., Baumgardt H., 2017, *MNRAS*, 471, 3668
- Spitzer L., 1987, in "Dynamical evolution of globular clusters", Princeton Univ. press, Princeton NJ
- Tang S.-Y., et al., 2019, *ApJ*, 877, 12
- Toomre A., Toomre J., 1972, *ApJ*, 178, 623